Experimental mechanical characterization of plastic-bonded explosives

Viet Dung Le · Michel Gratton · Michaël Caliez · Arnaud Frachon · Didier Picart

Abstract This article deals with the characterization of the static mechanical behavior of an energetic material. Due to its constituents (crystals and a polymeric binder), the behavior is complicated to model. A specific experimental protocol has been proposed in this article. It involves uniaxial tensile and compressive tests, compression under confinement and dynamic mechanical analysis. A constitutive law has been developed. The behavior is described using a Maxwell's model, in which all the components are influenced by an isotropic damage. The first component takes into account an elasto-plastic behavior. The yield stress evolution is described using a parabolic criterion and an isotropic hardening law. The plastic flow rule is non-associated. A linear visco-elastic behavior is used for the other components. Numerical simulations show that experimental data are quite well reproduced. The last part of the article is devoted to a discussion highlighting the future improvements.

Introduction

Energetic materials are often used under thermal and/or mechanical loading conditions. When modeling the response of these materials, it is necessary to have an in depth knowledge and characterization of the behavior. This article is about a material made of energetic crystals (octahydro-1,3,5,7-tetranitro-1,3,5,7-tetrazocine, HMX) mixed with a few percentage of a binder. An isostatic compaction process eliminates the initial porosity of the powder (Fig. 1), which results in a quasi-brittle concrete-like material, with the largest grains embedded in a "matrix" composed of the binder, the smallest crystals, and the residual porosity. The main difference with concretes is the strain-rate dependence which could be attributed to the small amount of polymeric binder.

Microscopic observations show a lot of micro-cracks inside or between crystals due to the high volume fraction of the solid phase and the pressure applied to compact the material.

During the 1980s, an extended database (several hundred experiments) was necessary to characterize this material [1]. Uniaxial compressive or tensile tests were applied at constant strain rate or stress rate loading conditions, with or without pressure confinement (triaxial experiments) or temperature variation. However, the surveillance of the possible aging of this material implies an accurate determination of the mechanical properties when this material is only available in small amounts after disassembling. Consequently, a reduced number of tests can be performed using small-sized samples. In this study, we have take advantage of the evolution of experimental techniques (machines, measurements) and numerical tools to propose new experiments and a constitutive law.

Many observations were published about PBX 9501, another pressed HMX-based plastic-bonded explosive composition. For tensile or compressive loading conditions, a non-linear increase of the uniaxial stress is obtained [2]. Once the maximum stress is reached, a decrease is registered. The strain at the maximum stress being close to 1% during compressive tests, a quasi-brittle behavior is exhibited. During tensile tests, the strain at the maximum

V. D. Le · M. Gratton · M. Caliez · A. Frachon
ENI Val de Loire, Laboratoire de Mécanique et Rhéologie,
Université F. Rabelais-Tours, Rue de la chocolaterie, BP 3410,
41034 Blois Cedex, France

D. Picart (✉)
CEA, DAM, Le Ripault, 37260 Monts, France
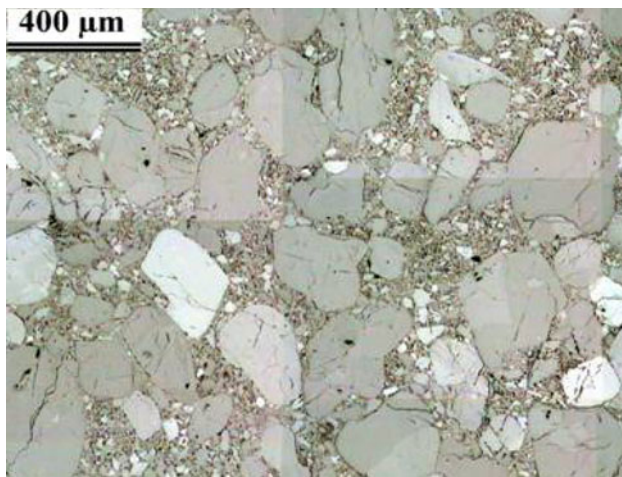e-mail: didier.picart@cea.fr

Fig. 1 Microstructure of the explosive composition. Micro-cracks are the consequence of the compaction process

stress was several times less than the one recorded during compressive experiments. The high volume fraction of the granular phase causes, first, the difference between compressive and tensile experiments and, second, the behavior observed at higher hydrostatic pressures [3, 4].

A more ductile behavior appears as the confining pressure increases. The brittle–ductile transition is obtained for a confining pressure above 20 MPa. A dependence of initial Young's modulus on the pressure was also noticed by Wiegand [3]. It is not clear how this dependence is a consequence of the increase of the glass transition temperature of the material, of the decrease of the initial porosity, or of the increase of internal surfaces where friction locks the relative displacements (contacts between crystals, closure of micro-cracks). For compressive and tensile experiments, strain rate and temperature dependences were observed [5–8].

The mode-I fracture process in PBX 9501 was investigated by Liu [9] using symmetric or asymmetric four-points bend tests and Brazilian tests. The process zone ahead of the crack has an extended size and cannot be described by the classical Griffith's theory.

In spite of this extended experimental database, only a little data is available in the literature about tensile behavior. However, this loading path is one of the most dramatic conditions which could lead to explosive part failure, for example, during disambling or cooling. On the other hand, the coupled influence of the strain rate, the temperature and the pressure has not been studied. Experiments were conducted using only a constant variation of the strain and without measurements of the transversal strain. As a consequence, dilatancy mechanism (well-known for soils, concretes, and geomaterials) was not determined and the time-dependent stress could not be separated from the total stress. A new experimental

protocol is proposed and detailed in the second part of this article. Experiments were designed to reduce the number of experiments and to conduct more informative tests. Tests were performed at room temperature with loading conditions ranging between 0 and 10 MPa for the mean pressure, and between 10^{-6} and 10^{-3} s^{-1} for the strain rate. The temperature dependence of the behavior is out of the scope of this article. In the third part of this article, the behavior is analyzed. Three main phenomena have been identified: residual strain, time dependence, and damage.

The dynamic and high pressure loading conditions leading to ignition, for example, during an impact, motivated research on the constitutive law of PBX 9501. The well-known Visco-SCRAM model [10] was a combination of the damage theory, denoted SCRAM, proposed by Dienes for brittle materials [11], and a linear visco-elastic Maxwell's model. The initial SCRAM approach was reduced by [10] to a constitutive law incorporating isotropic damage, in which evolution was related to the mean crack radius growth. A discussion on such damage laws can be found in [12]. The model was calibrated from quasi-static to dynamic loading conditions, and predictions were compared to displacement fields obtained using a few impact configurations [13–15]. Later, Hackett and Bennett [16] modified the crack growth to take into account the influence of the pressure, and the difference between tensile and compressive behaviors. An update of SCRAM has been recently proposed by Dienes et al. [17]. The crack distribution anisotropy is taken into account as well as the coalescence and the nucleation of penny-shaped cracks.

Some comments are now proposed about the previous constitutive laws. First, the pressure part of the stress was disconnected from the deviatoric one, except through the damage law. Maxwell's law was only devoted to the deviatoric part of the behavior. Consequently, simulations cannot capture, for example, the evolution of the initial elastic modulus obtained during triaxial tests for various confinement conditions. Second, the degradation mechanism was based on a mode-I failure model when shear localization (mode-II) is suspected to happen for dynamic conditions and/or for high confinement load. Finally, dilatancy or compaction of the material was not allowed. Even if some of the model parameters seemed to be related to the mesoscopic scale (mean crack radius, crack growth rate), an inverse method is necessary to determine these parameters using the macroscopic experimental database.

A constitutive law for our material was proposed [18], assuming a negligible visco-elasticity and describing the time dependence using a visco-plastic flow rule. This model reproduces the loading and the relaxation conditions. However, unloading and hysteretic behavior are poorly reproduced due to the absence of visco-elasticity.

The constitutive law proposed in this article is restricted to quasi-static loading conditions for which a lot of data are now available. A generalized Maxwell's model is adopted with an elasto-plastic and a visco-elastic coupling. Isotropic damage is assumed. It influences the entire model. The main differences between this work and the visco-SCRAM model are (1) the arrangement of the components, which are submitted to the same strain coming from the global equilibrium state and (2) a Maxwell's model applied to the total stress and not only to the deviatoric one.

The fourth and fifth parts of this article are devoted to a description of the constitutive law and comparisons between experimental and computed data. We deduce the limits and assets of this model, and the capability of a modified generalized Maxwell's model to reproduce the quasi-static mechanical behavior of this class of materials.

Experimental procedure

Standard tests made in various material directions shown an initial isotropic behavior. To ensure statistical validity and to check the dispersion level, each test reported in this article was repeated five times. Negative stress or strain values reported refer to compressive conditions on further figures.

Shape ratio of the samples

The specimen size was chosen to keep large dimensions compared to the internal material characteristic lengths (diameter of crystals). Samples were machined in several geometric shapes, which were more than 10 times the length of the material heterogeneity. Different diameters (Ø) and lengths (L) were tested using compressive experiments (cylindrical samples) to analyze the material homogeneity and the shape dependence of data. Figure 2 shows that, for a given geometry of the sample, all the curves are closed to each other. It demonstrates the homogeneity of the material properties.

The analysis proposed in Fig. 3 underlines the shape dependence of the data. One can see the maximum stress (σ_{max}) and the associated strain (ε_{peak}) as a function of the shape ratio (L/Ø). A value of 4/3 increases the stiffness of the longitudinal behavior. However, when the ratio exceeds two, this effect vanishes and an asymptote appears on the maximum stress. Nothing can be said about the strain. Several explanations were proposed such as the influence of friction on the end surfaces of the sample or the intersection of the shear plane with these surfaces [19]. Considering only the maximum stress (σ_{max}), a shape ratio of two is a good compromise for the compressive loading
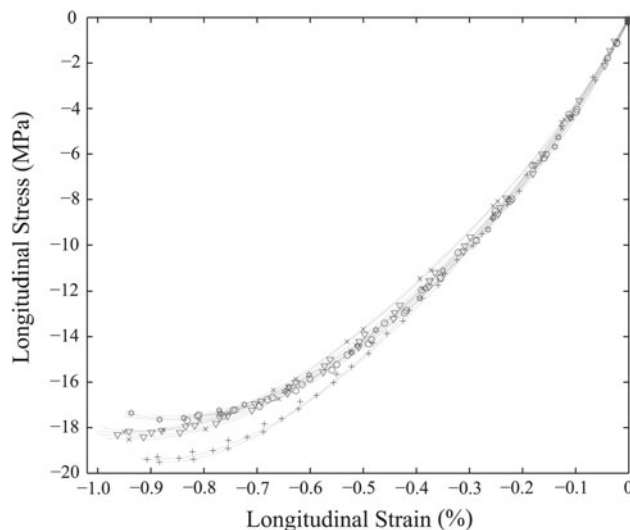

Fig. 2 Stress versus strain for compressive experiments ($\dot{\varepsilon} = 1.7 \times 10^{-4}$ s^{-1}) and different shape ratios (L/Ø): diameter 10 mm and length 20 mm (o), 12.5 and 25 mm (x), 15 and 30 mm (∇), 15 and 20 mm (+), 10 and 30 mm (✿)

paths. The adopted geometry was Ø10L20 mm^2 for uniaxial tests and Ø50L100 mm^2 for triaxial ones.

This study could be reproduced for tensile conditions. The brittle response in tension being highly influenced by initial geometric defaults of the experimental setup, a tied interface is currently being studied. Waiting for these results, dog-bone samples of 150-mm length with a rectangular cross section of 10 × 10 mm^2 were used.

Protocols

Samples were equipped with two opposite pairs of strain gauges. Gauges signals were averaged (after estimation of the strain heterogeneity) to provide the longitudinal and the
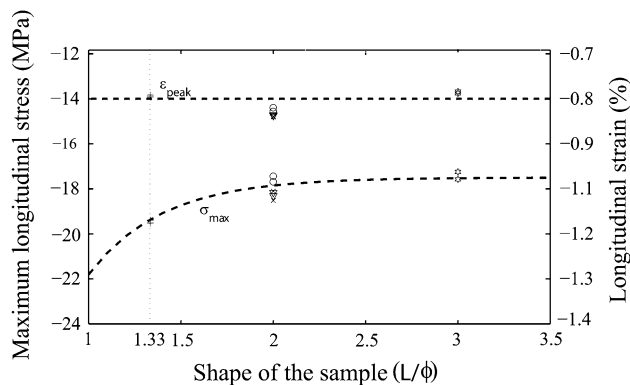

Fig. 3 Evolution of the maximum stress and of the peak strain for compressive tests ($\dot{\varepsilon} = 1.7 \times 10^{-4}$ s^{-1}) and various shape ratios (L/Ø): diameter 10 mm and length 20 mm (o), 12.5 and 25 mm (x), 15 and 30 mm (∇), 15 and 20 mm (+), 10 and 30 mm (✿)

transversal strains during the test. The longitudinal strain rate imposed during experiments was obtained by controlling one of the two longitudinal gauges. Stress was deduced from the force measured by a sensor. The triaxial compression experiments were done using geomaterials characterization tool (hermetic cell, pressure controller, and water). The first stage of the loading program was a hydrostatic loading condition (0, 5, or 10 MPa). Then, an uniaxial load was applied.

One of the main improvements to the usual testing procedure was the use of cyclic loading conditions (five to six cycles) to underline possible evolutions of the elastic properties. After unloading and a delay to recover time-independent data, we measured the residual strains. The viscosity was observed either (1) using uniaxial tests for different loading strain rates (from 3×10^{-6} to 10^{-3} s^{-1}) or (2) using relaxations during cyclic loading conditions. The test was controlled for 30 min (resp. 50 min) during the relaxation condition (resp. the recovery condition) (Fig. 4). Relaxation times were defined to guarantee an almost complete relaxation of the stress. We took into account a maximum test duration of 8 h imposed for safety reasons.

A Dynamic Mechanical Analysis apparatus (denoted DMA in this article) was also used in a tensile-compressive mode with samples of 50-mm long and a cross section of 5×5 mm^2. Samples were glued to the platens.

Global trends of the behavior

Figures 5 and 6 entail arrangements for the mechanical tests and show some of the main features of the material. A non-linear behavior is observed whatever the loading conditions. A quasi-brittle behavior is observed during tensile experiments (Fig. 6). A more ductile one is obtained during triaxial experiments. The maximum stress is influenced by
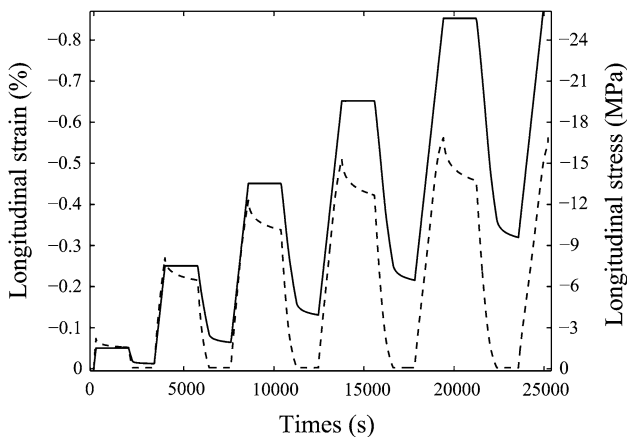

Fig. 4 Longitudinal stress (*dashed line*) and strain (*line*) versus time: an example of relaxation and recovery loading conditions
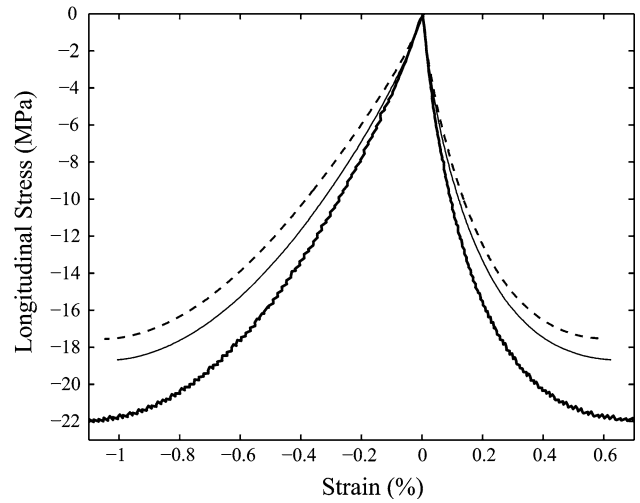

Fig. 5 Influence of the strain rate (compressive tests): 8.3×10^{-4} (*bold line*), 3.3×10^{-5} (*line*), and 3.3×10^{-6} s^{-1} (*dashed line*)
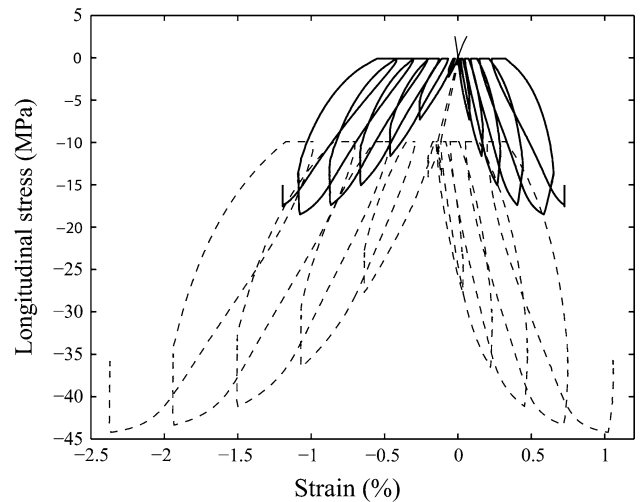

Fig. 6 Influence of the pressure and difference between compressive and tensile loading conditions: tensile (*line*), compressive (*bold line*) and tri-axial experiments (*dashed line*)

the hydrostatic pressure. Finally, a hysteretic response is obtained for cyclic loading conditions. These observations show that our material behaves like a concrete due to its quasi-compact granular microstructure. The influence of internal friction can be suspected as well as damage by micro-cracks nucleation and coalescence. Residual strains are registered after unloading and recovery. Optical observations of the microstructure shown that grains are not significantly deforms, irreversibility being associated to local damage. However, a different assumption will be used to model the macroscopic behavior.

The time dependence of the behavior was observed first comparing the maximum stress during constant strain rate tests (Fig. 5). Linear visco-elastic behavior was characterized using DMA experiments. The material was submitted
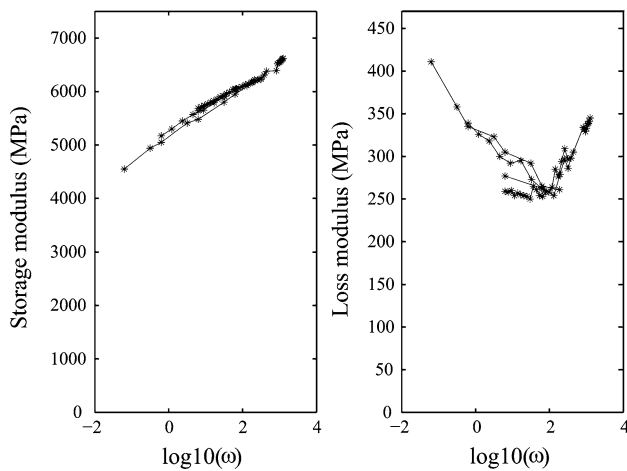
Fig. 7 Experimental data recorded during Dynamic Mechanical Analysis experiments (DMA). Storage modulus (*left*) and loss modulus (*right*) versus the logarithm of $2\pi f$, where f is the frequency

to a sinusoidal load with small amplitude ($\varepsilon_0 = 10^{-4}$), the linearity of the behavior being previously controlled. The range of frequencies goes from 0.004 to 200 Hz and the quadratic average strain rate range from 2×10^{-6} to 1×10^{-1} s^{-1}. Visco-elastic storage (E_{stor}) and loss (E_{loss}) modules were determined (Fig. 7).

The broad loops observed on Fig. 6 and the decrease of the stress (resp. the strain) during the relaxation (resp. recovery) conditions are attributed to visco-elasticity, assuming that irreversible mechanisms are locked during unloading. However, the asymmetry of the response obtained during a creep-recovery test suggests that another time-dependent mechanism must be added to linear visco-elasticity (Fig. 8).

Figure 9 shows a comparison between (1) a constant strain rate experiment and (2) a test with the same strain
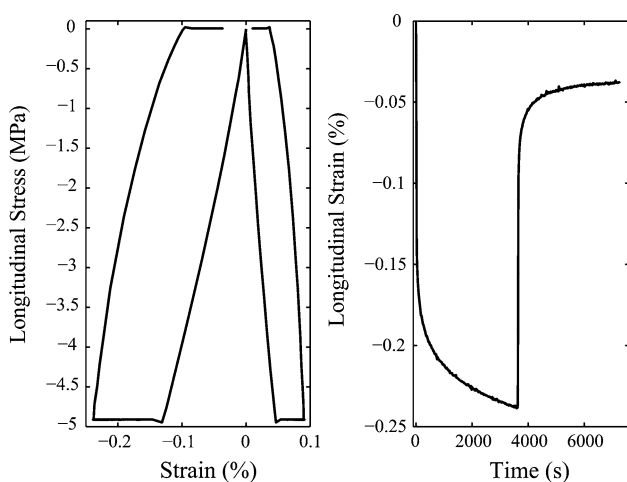

Fig. 9 Stress versus longitudinal and transversal strains for a constant strain rate equal to 3.3×10^{-5} s^{-1} (*bold lines*) and the same test interrupted by cycles (*line*). For each test, the two gauges glued on the lateral surface of the sample provided two longitudinal (respectively transversal) strain measurements (*dashed or not dashed lines*)

rate loading/unloading conditions and relaxation/recovery setup. The result of the second test is embedded below the first one, which will be referred to as the "cover curve" in this article. The same observation was done using different strain rate conditions or cycles without relaxation and recovery conditions.

In addition, the time-dependent stress can be drawn for three confining pressures during relaxation. The same strain amplitude is chosen for each test. Figure 10 shows the pressure dependence of the time-dependent stress. This phenomenon is consistent with the pressure dependence of the initial elastic modulus described later in this article (Fig. 15).

Fig. 8 Experimental data recorded during a creep-recovery test. Stress versus longitudinal and transversal strains (*left*) and strain versus time (*right*)
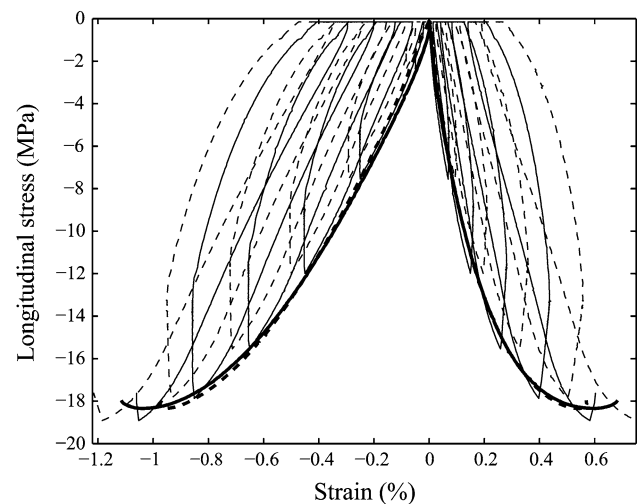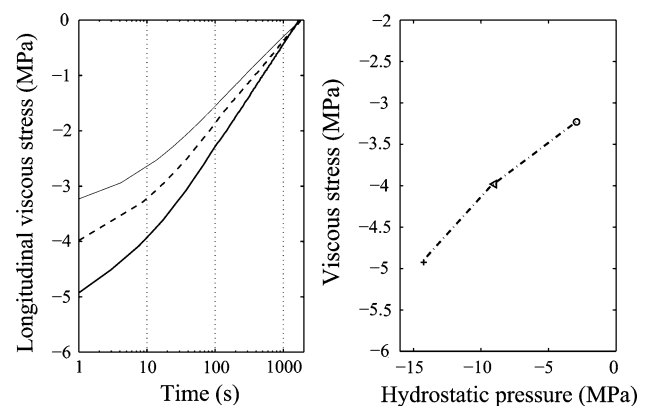

Fig. 10 Three relaxation curves recorded during compressive tests with the same strain but different confinements (compressive test: *line or circles*; confinement of 5 MPa: *dashed line* or Δ; confinement of 10 MPa: *bolded line* or $+$). Influence of the pressure on the time-dependent stress (*left*) and initial amplitude of the time-dependent stress (*right*)

The same analysis can be done using the recovery conditions. Figure 11 (left) gives a comparison between two records obtained for two confining pressures (5 and 10 MPa). These conditions were chosen because the level of the stress at the end of the relaxation and the residual strain were approximately the same. However, strain versus time curves are different. A dependence on the strain and/or the damage amplitudes is suspected (Fig. 11 right).

A master curve can be drawn for a given confinement but different strain rates, joining all the stress–strain data measured at the ends of relaxation times (Fig. 12). This observation shows that a hardening mechanism is at work. On the other hand, residual strains are used to observe the volumic and deviatoric parts of the behavior (Fig. 13). When the volume increases for tensile tests, a more complicated behavior is deduced from compressive experiments, showing an influence of the confining pressure. This

Fig. 13 Volumic versus deviatoric residual strains. Influence of the pressure: tensile experiment ($*$), compressive experiment (o), and tri-axial experiments with a confining pressure of 5 ($\triangleleft$) and 10 MPa (+)
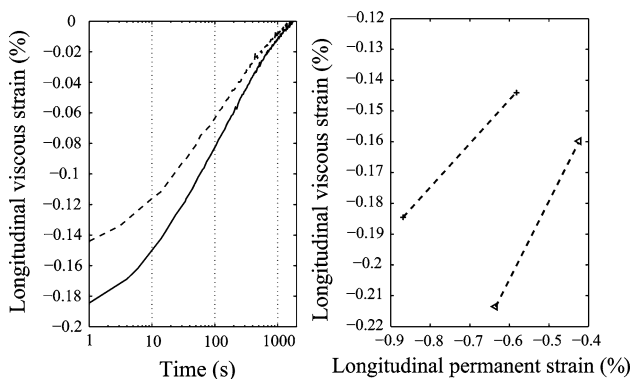

Fig. 11 Two recovery curves (left) recorded during a tri-axial experiment with a confinement of 10 MPa, for a residual strain after recovery equal to 0.58% (dashed line) or equal to 0.87% (bold line). The viscous strain is reported (right) versus residual strains for 5 and 10 MPa of confinement
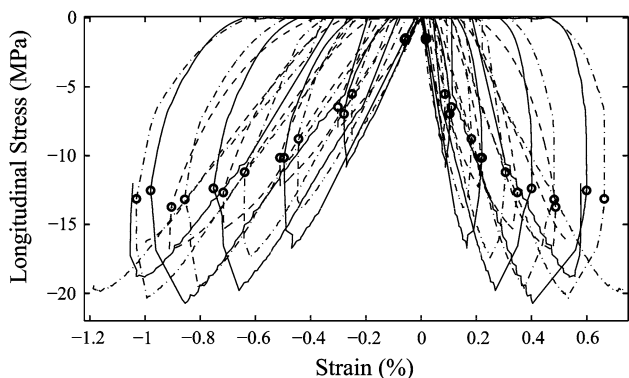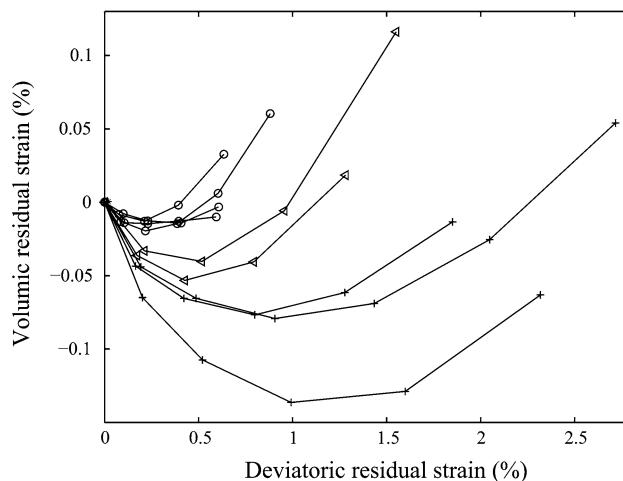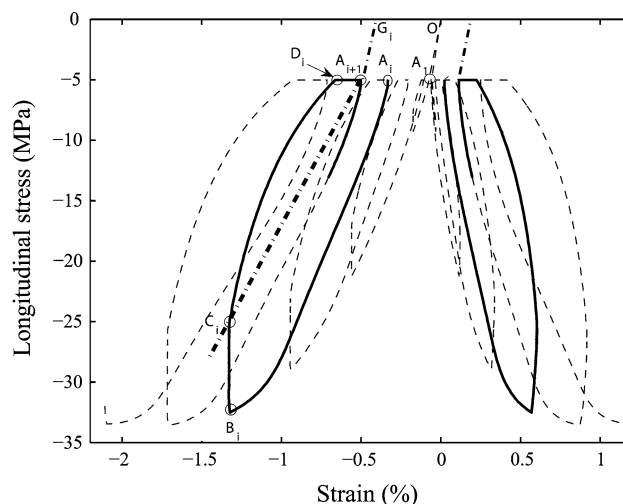

Fig. 14 Stress versus strains for a tri-axial experiment with a confining pressure of 5 MPa of pressure. Data were analyzed using dots A_i to D_i. Bolded line highlights a cyclic load involving loading (A_iB_i), relaxation (B_iC_i), unloading (C_iD_i), and recovery conditions (D_iA_{i+1})

Fig. 12 Relaxed stress (circles) for each cycle and different strain rates (uniaxial compressive tests): 3.3×10^{-3} (——), 8.3×10^{-4} (— · —), and 3.3×10^{-6} s^{-1} (— —)

mechanism, called here as the "compaction-dilatancy" phenomenon, is well-known for rocks, soils, and concrete-like materials.

Loops observed on Figs. 6, 9, or 12 can be described by a set of data $A_iB_iC_iD_iA_{i+1}$ as on Fig. 14. The slope of the line C_iA_{i+1} gives the current elastic modulus when the stress is relaxed. One can see on Fig. 15 a dependence of the initial modulus to the confining pressure. It can be due to the closing of a part of the residual porosity or of micro-cracks created during the process. Second, a decrease of the modulus is observed, pointing out to a damage mechanism usually associated to an increase of the positive strain.
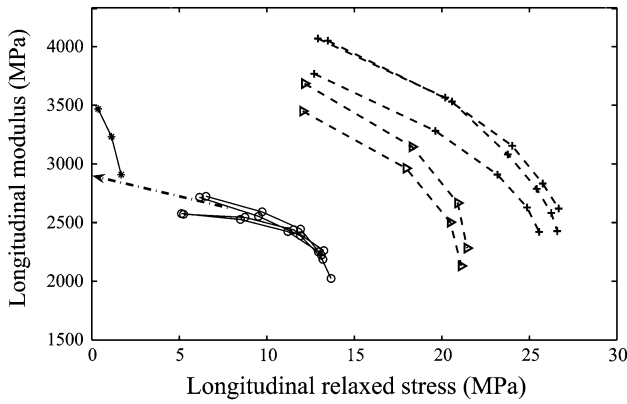
Fig. 15 Secant Young's modules (slope of the line C_iA_{i+1} on Fig. 14) for tensile experiment (∗), compressive experiments (o), and tri-axial experiments with a confining pressure of 5 (◁) and 10 MPa (+). The modules decrease with the relaxed stress. There extrapolations to the origin of the graph give initial Young's modules

Many observations of the microstructure confirmed this deduction and shown that damage develops by micro-cracking during poorly confined pressure conditions.

This part of the article has shown that the behavior of pressed energetic materials is complicated. The constitutive law recently proposed for this energetic material was based on an elastic visco-plastic model. It takes into account the pressure and the damage dependences [18]. However, if the global trends of the behavior are reproduced, this model fails in representing the hysteretic behavior and the elastic time dependence. In this article, this constitutive law is modified. The visco-elastic data and the curve joining the relaxed data for all the strain rates (Fig. 12) guided us to a Maxwell's model incorporating an elasto-plastic component (Fig. 16). For the sake of simplicity, the dependence of the visco-elasticity on the
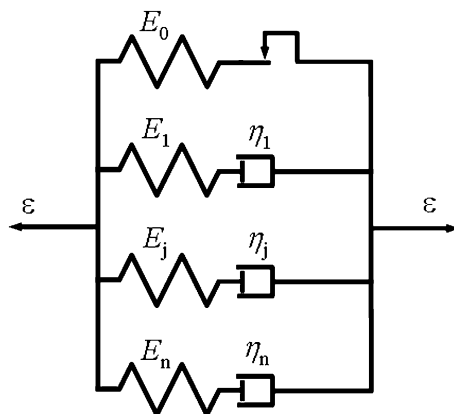

Fig. 16 A schematic diagram of the visco-elastic plastic model proposed in this article

pressure, the damage or the residual strain is omitted. The constitutive law is now detailed.

Constitutive law

The macroscopic stress tensor $\boldsymbol{\sigma}$ is defined as the sum of the stress of the first time-independent elasto-plastic component ($\boldsymbol{\sigma}_{ep}$) and of the time-dependent components ($\boldsymbol{\sigma}_j$) using the following relation:

$$\boldsymbol{\sigma} = \boldsymbol{\sigma}_{ep} + \sum_{j=1}^{n} \boldsymbol{\sigma}_j, \quad \boldsymbol{\varepsilon} = \boldsymbol{\varepsilon}_{ep}^e + \boldsymbol{\varepsilon}_{ep}^p = \boldsymbol{\varepsilon}_j^e + \boldsymbol{\varepsilon}_j^v \tag{1}$$

An additive decomposition is assumed for the strain, denoted $\boldsymbol{\varepsilon}$, of each component between an elastic part and a plastic or time-dependent one. The model is now described in the following paragraphs. An analysis of thermodynamic requirements is proposed further (see "Annex").

Elasto-plastic component

A linear elastic behavior is supposed, with a dependence on the damage level d, using the following equation:

$$\boldsymbol{\sigma}_{ep} = (1 - d)\boldsymbol{D}_0^{el} : \boldsymbol{\varepsilon}_{ep}^e, \tag{2}$$

where $\boldsymbol{D}_0^{el}$ is the initial elastic tensor. C_i on Fig. 14 defines the yield surface of the plastic component because the visco-elastic part is stress-free. C_iA_{i+1} gives the elastic modulus E_{ep}. $A_{i+1}G_i$, whose slope is assumed to be $E_{ep}/(1 - 2v)$, gives the plastic strain (measurements show a Poisson's ratio of 0.3 and a constant bulk modulus). A mean Young's modulus equal to 2,900 MPa is determined using unconfined compressive tests on Fig. 15. This assumption has some consequences on the damage determination (see later).

Due to the lack of data on the hardening mechanism, a unique isotropic hardening parameter, denoted k, is introduced in the constitutive law. The softening behavior observed during the compressive tests is ignored (tensile experiments have shown a brittle failure process). Consequently, a saturation of the hardening mechanism at the maximum stress is assumed.

A review of the main criteria used to describe isotropic plasticity was presented in [18]. The chosen non-linear plasticity criterion is given by the following relation (Fig. 17):

$$f(Q_{ep}, P_{ep}, k) = \sqrt{Q_{ep}^2 + b(k)P_{ep}} - k, \quad b(k) = \frac{k^2}{X(k)},$$

$$X(k) = X_0 + (X_m - X_0)\frac{k - k_0}{k_m - k_0}, \tag{3}$$

where $Q_{ep} = \sqrt{(1/3)\boldsymbol{\sigma}_{ep}^D : \boldsymbol{\sigma}_{ep}^D}$ is the octahedral stress, $\boldsymbol{\sigma}_{ep}^D$ is the deviatoric stress and P_{ep} is the pressure. The
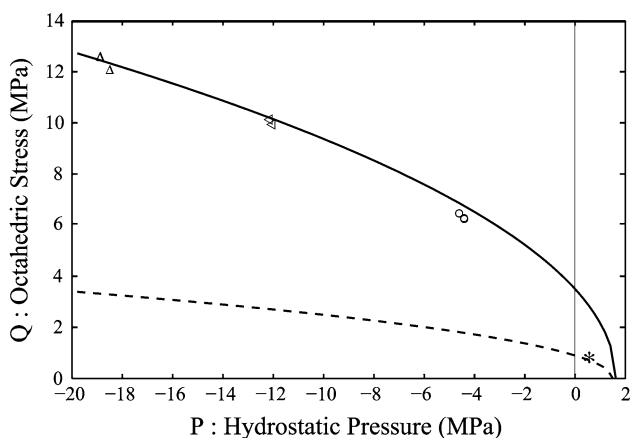
Fig. 17 Initial (*dashed line*) and saturated yield criterion (*bold line*) in the relaxed stress plane (P, Q). Symbols refer to tensile experiment (∗), compressive experiment (o) and tri-axial experiments with a confining pressure of 5 (◁) and 10 MPa (Δ)

Fig. 18 Hardening parameter k versus the effective plastic strain p [tensile experiment (∗), compressive experiment (o), and tri-axial experiments with a confining pressure of 5 (◁) and 10 MPa (+)]. Model is given using *dashed line*

following guidelines help for the determination of $X(k)$. The yield curves must not cross themselves in the P–Q plane, each one being embedded in those of higher levels, all of them being embedded in the maximum curve defined by the maximum relaxed stress recorded for several confining pressures.

Elementary algebra shows that the proposed relation satisfies the previous requirements. k_0, X_0, k_m, and X_m are four material parameters. The two parameters X_m and k_m are determined using the maximum yield stress curve. The following values are obtained: $X_m = 1.62$ MPa and $k_m = 3.45$ MPa.

The hardening parameter k is related to the effective plastic strain, denoted p. If it could be possible to take into account a plastic volumic part in p [18, 20], this solution couples hardening to dilatancy. As a consequence, an approximation in dilatancy prediction induces error on the hardening description. Such approach has not been adopted. The cumulated deviatoric plastic strain p is chosen to drive the hardening parameter k (Fig. 18). For the hardening law, the following hyperbolic empirical relation is used:

$$k = k_0 + (k_m - k_0)\left(1 - \frac{1}{1 + c_1 p + c_2 p^2}\right) \quad (4)$$

The four parameters c_1, c_2, k_0, and X_0 are determined using an optimization process applied to three sets of data: the response recorded during three-points bend tests, the compressive tests (with and without confinement) and the hardening curves shown in Fig. 18. The following values are obtained: $X_0 = 1.5$ MPa, $k_0 = 1$ MPa, $c_1 = 450$ and $c_2 = 1.4 \times 10^5$.
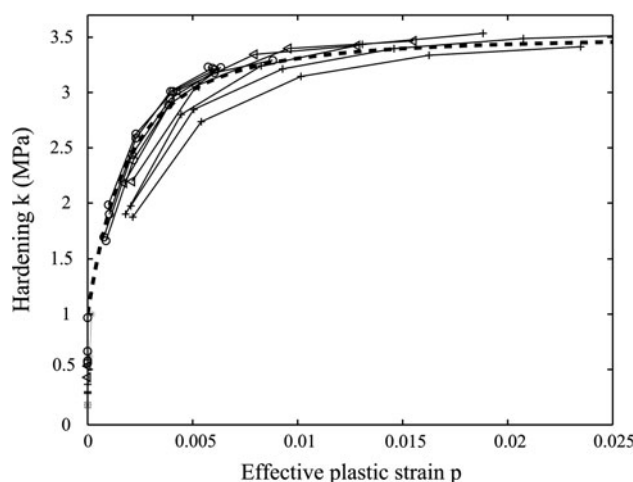
The flow rule is given by:

$$\dot{\boldsymbol{\varepsilon}}_{ep}^{p} = \dot{\lambda}\left(\frac{\boldsymbol{\sigma}_{ep}^{D}}{3Q_{ep}} + \frac{\beta}{3}\boldsymbol{I}\right) \cdot \sqrt{\frac{3}{(1+\beta^2)}}, \quad \beta = \frac{\dot{\varepsilon}_{ep}^{pV}}{\dot{\varepsilon}_{ep}^{pD}},$$

$$\dot{\varepsilon}_{ep}^{pV} = \mathrm{tr}(\dot{\boldsymbol{\varepsilon}}_{ep}^{p}), \quad \dot{\varepsilon}_{ep}^{pD} = \sqrt{3\dot{\boldsymbol{\varepsilon}}_{ep}^{pD} : \dot{\boldsymbol{\varepsilon}}_{ep}^{pD}} \quad (5)$$

where $\dot{\lambda}$ is the plastic multiplier and $\dot{\boldsymbol{\varepsilon}}_{ep}^{pD}$ is the deviatoric plastic strain rate tensor. The parameter β is determined knowing the slopes of the curves shown on Fig. 13. A dependence on the cumulated deviatoric plastic strain p and on the pressure P_{ep} was observed and taken into account using the following equation:

$$\beta = C_0 + a_1\left(1 + \mathrm{e}^{a_2 P_{ep}}\right) + a_3 P_{ep} + b\ln(1 + cp), \quad (6)$$

where C_0, a_1, a_2, a_3, b, and c are five parameters.

Visco-elastic components

The damage is assumed to influence all the components of the constitutive law. Moreover, relaxation times, denoted τ_j, are unchanged and the same values are used for spherical or deviatoric visco-elasticity. As a consequence, each visco-elastic component is described by the following linear first order differential equation:

$$\dot{\boldsymbol{\sigma}}_j^{ve} + \left(\frac{1}{\tau_j} + \frac{\dot{d}}{1-d}\right)\boldsymbol{\sigma}_j^{ve} = (1-d)\boldsymbol{K}_{0j}^{ve} : \dot{\boldsymbol{\varepsilon}}, \quad (7)$$

where $\boldsymbol{K}_{0j}^{ve}$ is the elastic tensor of each visco-elastic component. The Poisson's ratios of the elastic and time-dependent part of each component are equal to $\upsilon^{ve} = 0.42$.

For a one-dimensional application of the model (for example, to use DMA measurements), the material response can be split into an in-phase part (related to the storage modulus E_{stor}) and an out-phase part (related to the

loss modulus E_{loss}). These modules are related to Young's modulus and the visco-elastic parameters using the following relations:

$$E_{stor} = E_{ep} + \sum_{j=1}^{n} E_j \frac{(\tau_j \cdot \omega)^2}{1 + (\tau_j \cdot \omega)^2},$$

$$E_{loss} = \sum_{j=1}^{n} E_j \frac{(\tau_j \cdot \omega)}{1 + (\tau_j \cdot \omega)^2} \tag{8}$$

where $\tau_j = \eta_j/E_j$, η_j are the viscosities and ω is equal to 2π multiplied by the frequency. Ten visco-elastic components are used, the relaxation times τ_j being linearly distributed in the logarithmic time domain between 3,720 and 0.0005 s. The modulus E_0 previously determined ($E_0 = 2,900$ MPa) is lower than the lowest storage modulus measured (around 4,500 MPa). E_0 is then supposed to be the long-term response of the material. Moreover, the relaxation curves obtained during compressive tests with cycles have been used to calibrate the short-term response of the model. Visco-elastic parameters are summarized in the Table 1.

Damage

Experimental data show that Young's modulus decreases as the positive principal strain increases (Fig. 19). The most probable damage mechanism is the nucleation and the growth of internal micro-defects (cavities, cracks) with extension [21–26]. In the proposed constitutive law, the damage amplitude d is defined as:

$$d = \frac{E_0 - E}{E_0}, \quad d = \left(d_1 \underbrace{\sup}_{\text{time}} \left(\max_{I=1\,\text{to}\,3} \langle \varepsilon_I \rangle_+ \right) + d_2 \right)$$

$$\times \left(1 - \frac{1}{1 + d_3 \cdot \underbrace{\sup}_{\text{time}} \left(\max_{I=1\,\text{to}\,3} \langle \varepsilon_I \rangle_+ \right)} \right), \tag{9}$$

where E_0 and E are the initial and current Young's modules. An hyperbolic relation is used to relate d to the maximum positive principal strain, denoted $\max\langle \varepsilon_I \rangle_+$. d_1, d_2, and d_3 are three parameters. A comparison between Eq. 9 and experimental data is shown in Fig. 19. One can see that the model is determined using the uniaxial
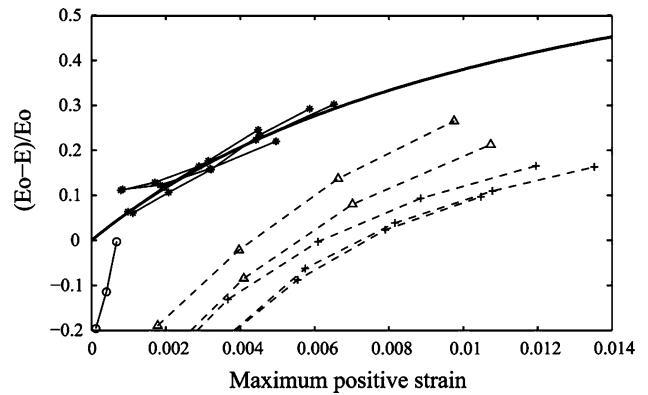

Fig. 19 Damage versus the maximum positive strain. Tensile experiment (∗), compressive experiment (o), and tri-axial experiments with a confining pressure of 5 (Δ) and 10 MPa (+)

compressive measurements. The pressure dependence of the initial Young's modulus is neglected for the sake of simplicity. We have determined the following values: $d_1 = 3$, $d_2 = 1$, and $d_3 = 100$.

Discussion

The constitutive law has been implemented into MATLAB software and the finite element code ABAQUS/Standard. Figure 20 shows a comparison between experimental data, the one-dimensional model, and simulations using ABAQUS. A detailed analysis outlines small differences which are attributed to the choice of equal Poisson's ratios for the elasto-plastic component and the visco-elastic ones. In the future, the three-dimensional interactions of the components should be carefully characterized to improve the model's accuracy.

Figures 21 and 22 show that the linear visco-elasticity is able to reproduce the material behavior for small strain amplitude. For compressive tests with and without confinement and with unloading cycles, relaxation and recovery conditions, the proposed flow rule is confirmed. The residual transversal strain is correctly reproduced. The hardening law and the plastic yield surface have been accurately fitted using these data. Loading and unloading behaviors are reproduced in the longitudinal direction but transversal loops are underestimated; thus, highlighting the influence of the internal friction or/and the damage.

Table 1 Visco-elastic parameters

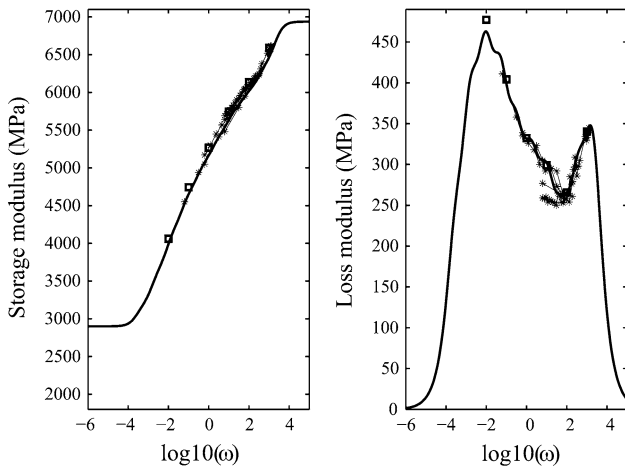| j	1	2	3	4	5	6	7	8	9	10
τ (s)	5×10^{-4}	29×10^{-4}	168×10^{-4}	0.098	0.567	3.28	19.1	110	641	3,720
E_j (MPa)	546	336	240	348	492	384	492	552	492	288

Fig. 20 Comparison between DMA data (∗) and the model with 10 components (*solid line* for a Matlab implementation of the model and *squares* for Abaqus finite element code implementation of the model)
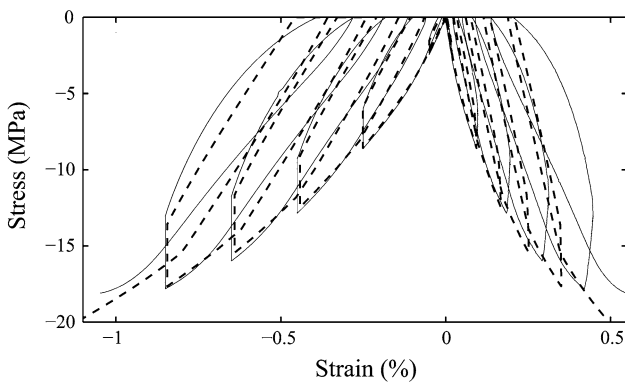

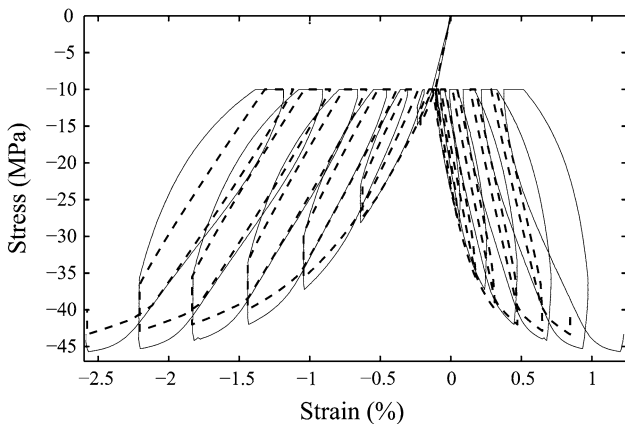**Fig. 21** Model (*dashed line*) versus data (*line*) for a compressive test

Fig. 22 Model (*dashed line*) versus experiment (*line*) for the compressive test with 10 MPa of confinement

The choice of an isotropic hardening mechanism is questionable.

Differences increase with the confinement or the high plastic strain level. The visco-elastic stress amplitude is
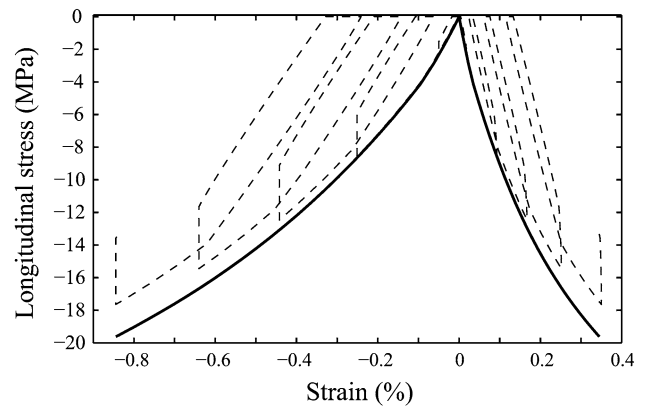

Fig. 23 Computed constant strain rate loading (*bolded line*) versus computed multiple cycled response (*dashed line*) for a compressive test

numerically underestimated. Both unloading–loading conditions and time response during recoveries are poorly reproduced. Finally, the model does not correctly describe the data shown on Fig. 9 (Fig. 23). Many parameter values were attempted to correct the constant strain rate prediction, but unsuccessfully. Our opinion is that it is now necessary to (1) characterize the different Poisson's ratios of the constitutive law, (2) to deduce how non-linear visco-elasticity could improve numerical results, and (3) to analyze different rheological approaches (for example, a Maxwell's model only for the deviatoric part of the behavior).

Conclusion

A new experimental protocol was carried out to characterize in depth the behavior of a pressed plastic-bonded explosive composition. The influence of the pressure, the viscosity, and the damage have been observed and discussed. This material behaves in a similar way than concrete-like materials, due to its high volume fraction of solid.

A visco-elastic plastic constitutive law has been proposed, based on a Maxwell's model associated to an elasto-plastic component. Comparisons between data and numerical results have shown that the material description proposed in [18] has been improved. However, the following remarks outline future works. The model reproduces the relaxed data. However, the constant strain rate data are not the cover curve of the corresponding cyclic tests, as was experimentally observed. The shape of the hysteretic loops, the behavior observed during creep-recovery experiments, the influence of the pressure on the material relaxation and the plastic strain dependence observed during recovery show the need of a non-linear visco-elasticity and/or a visco-plastic mechanism. It is

necessary to go into a detail characterization of the Poisson's ratios of the constitutive law to understand how longitudinal and transversal behaviors interact. A pressure dependence of Young's modulus must be incorporated as well as an anisotropic description of the induced damage. An isotropic plastic hardening mechanism has been proposed which is the simplest assumption. The case of kinematic hardening must be re-examined using alternating tensile-compressive tests.

Appendix: Thermodynamical requirements

Only small strain amplitude is taken into account, leading to an assumed constant density of the material. As a consequence, the intrinsic dissipation reads, in a general way:

$$\omega = \boldsymbol{\sigma} : \dot{\boldsymbol{\varepsilon}} - \dot{\psi} \geq 0 \quad \forall \dot{\boldsymbol{\varepsilon}}, \quad \forall \text{ state variables}$$

with $\dot{\psi}$ the per unit volume free energy. The following set of internal variables is proposed: $\{\boldsymbol{\varepsilon}, \boldsymbol{\varepsilon}_{ep}^p, \boldsymbol{\varepsilon}_j^v, d, p\}$, given by:

$$\psi\left(\boldsymbol{\varepsilon}, \boldsymbol{\varepsilon}_{ep}^p, \boldsymbol{\varepsilon}_j^v, d, p\right) = (1 - d)\left(\frac{1}{2}(\boldsymbol{\varepsilon} - \boldsymbol{\varepsilon}_{ep}^p) : \boldsymbol{D}_0^{el} : (\boldsymbol{\varepsilon} - \boldsymbol{\varepsilon}_{ep}^p)\right.$$
$$\left. + \frac{1}{2}\sum_{j=1}^n (\boldsymbol{\varepsilon} - \boldsymbol{\varepsilon}_j^v) : \boldsymbol{K}_{0j}^{vel} : (\boldsymbol{\varepsilon} - \boldsymbol{\varepsilon}_j^v)\right) + \bar{\psi}(p) + \psi_0$$

Taking the assumption $\boldsymbol{\sigma} = \partial\psi/\partial\boldsymbol{\varepsilon}$ gives:

$$\varpi = (1 - d)\boldsymbol{D}_0^{el} : (\boldsymbol{\varepsilon} - \boldsymbol{\varepsilon}_{ep}^p) : \dot{\boldsymbol{\varepsilon}}_{ep}^p + (1 - d)$$
$$\times \sum_{j=1}^n \boldsymbol{K}_{0j}^{vel} : (\boldsymbol{\varepsilon} - \boldsymbol{\varepsilon}_j^v) : \dot{\boldsymbol{\varepsilon}}_j^v - \bar{\psi}'(\boldsymbol{p})\dot{\boldsymbol{p}}$$
$$+ \left(\frac{1}{2}(\boldsymbol{\varepsilon} - \boldsymbol{\varepsilon}_{ep}^p) : \boldsymbol{D}_0^{el} : (\boldsymbol{\varepsilon} - \boldsymbol{\varepsilon}_{ep}^p)\right.$$
$$\left. + \frac{1}{2}\sum_{j=1}^n (\boldsymbol{\varepsilon} - \boldsymbol{\varepsilon}_j^v) : \boldsymbol{K}_{0j}^{vel} : (\boldsymbol{\varepsilon} - \boldsymbol{\varepsilon}_j^v)\right)\dot{d} \geq 0$$
$$\forall\left(\boldsymbol{\varepsilon}, \dot{\boldsymbol{\varepsilon}}, \boldsymbol{\varepsilon}_{ep}^p, \boldsymbol{\varepsilon}_j^v, d, p\right)$$

and

$$\boldsymbol{\sigma}_{ep} : \dot{\boldsymbol{\varepsilon}}_{ep}^p - \dot{\bar{\psi}}(p) + \sum_j \boldsymbol{\sigma}_j : (\dot{\boldsymbol{\varepsilon}} - \dot{\boldsymbol{\varepsilon}}_j^e) - \frac{\partial\psi}{\partial d}\dot{d} \geq 0$$

Plasticity, visco-elasticity, and damage are uncoupled. The two last terms of the previous equation are positive due to the quadratic form of ψ. Consequently, only the elasto-plastic dissipation must be studied. It comes from the model that:
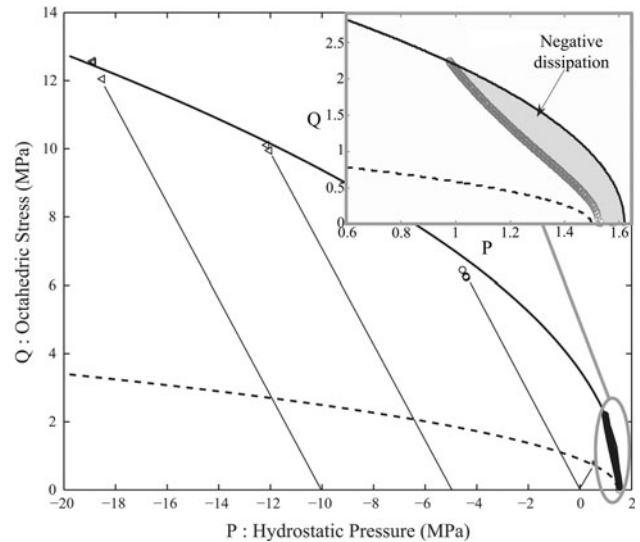
$$Q_{ep} + \beta(p, P_{ep})P_{ep} - k(p) + k_0 \geq 0$$

Fig. 24 Location of negative plastic dissipation in the (P, Q) stress plane. Negative dissipation occurs far from the failure stress recorded during tensile experiments

The analytical demonstration of this equation is hardly tractable due to the complicated forms of $\beta(p, P_{ep})$ and $k(p)$. Thereby a numerical method has been chosen. Only a small negative dissipation zone appears on Fig. 24 in the extension domain. Failure is reached before this zone.

References

1. Belmas R, Reynaud J, Sorel J (2004) Propellants Explos Pyrotech 7:8
2. Wiegand DA (1998) In: Proceedings of the 11th international symposium detonation, Snowmass, USA, pp 744–750, ONR 333000-5
3. Wiegand DA (1999) In: APS topical conference on shock compression condensed matter. 2000 AIP conference proceedings, Snowbird, USA, pp 675–678
4. Wiegand DA, Reddingius B (2003) In: APS topical conference on shock compression condensed matter. 2004 AIP conference proceedings, Portland, USA, pp 812–815
5. Funk DJ, Laabs GW, Peterson PD, Asay BW (1995) In: APS topical conference on shock compressed condensed matter. 1996 AIP conference proceedings, Seattle, USA, pp 145–148
6. Gray III GT, Blumenthal WR, Idar DJ, Cady CM (1997) In: APS topical conference on shock compression condensed matter. 1998 AIP conference proceedings, Amherts, USA, pp 583–586
7. Gray III GT, Idar DJ, Blumenthal WR, Cady CM, Peterson PD (1998) In: Proceedings of the 11th international symposium detonation, Snowmass, USA, pp 76–84, ONR 333000-5
8. Idar DJ, Thompson DG, Gray III GT, Blumenthal WR, Cady CM, Peterson PD, Roemer EL, Wright WJ, Jacquez BL (2001) In: APS topical conference on shock compression condensed matter. 2002 AIP conference proceedings, Atlanta, USA, pp 821–824
9. Liu C (2002) In: APS topical conference on shock compression condensed matter. 2003 AIP conference proceedings, Portland, USA, pp 786–791

10. Bennett JG, Haberman KS, Johnson JN, Asay BW, Henson BF (1998) J Mech Phys Solids 46:2303

11. Dienes JK (1996) In: Lee D et al (eds) High pressure shock compression of solids II. Springer, New York

12. Dienes JK, Kershner JD (1998) In: Proceedings of the 11th international symposium detonation, Snowmass, USA, pp 717–724, ONR 333000-5

13. Asay BW, Dickson PM, Henson B, Fugard CS, Funk DJ, Idar DJ (1998) In: Proceedings of the 11th international symposium detonation, Snowmass, USA, pp 781–787, ONR 333000-5

14. Clancy SP, Johnson JN, Burkett MW (1998) In: Proceedings of the 11th international symposium detonation, Snowmass, USA, pp 3–11, ONR 333000-5

15. Scammon RJ, Browning RV, Middleditch J, Dienes JK, Haberman KS, Bennett JG (1998) In: Proceedings of the 11th international symposium detonation, Snowmass, USA, pp 111–118, ONR 333000-5

16. Hackett RM, Bennett JG (2000) Int J Numer Math Eng 49:1191

17. Dienes JK, Zuo QH, Kershner JD (2006) J Mech Phys Solids 54:1237

18. Rja Fi Allah S (2006) PhD thesis, Université François Rabelais de Tours (in French)

19. Williamson DM (2006) PhD thesis, Magdalene College, Cambridge

20. Nova R (1982) In: Proceedings of the international workshop on constitutive behavior of soils, Villard de Lans, France, pp 289–309, published in 1984

21. Dragon A, Halm D, Désoyer T (2000) Comput Methods Appl Mech Eng 183:331

22. Halm D, Dragon A (1998) Eur J Mech A 17:439

23. Mazars J (1981) In: Proceedings of the international conference of fracture, Cannes, France, pp 1499–1506

24. Mazars J (1984) PhD thesis, Université Pierre et Marie Curie–Paris 6 (in French)

25. Mazars J (1986) Eng Fract Mech 25:729

26. Mazars J, Ragueneau F, Pijaudier-Cabot G (2002) In: Allix O, Hild F (eds) Continuum damage mechanics of materials and structures. Elsevier Science Ltd, Oxford